Journal of NUCLEAR SCIENCE and TECHNOLOGY, Vol. 42, No. 2, p. 225–232 (February 2005)

ORIGINAL PAPER

Microstructural Characterization of SCC Crack Tip and Oxide Film for SUS 316 Stainless Steel in Simulated PWR Primary Water at 320°C

Takumi TERACHI*, Katsuhiko FUJII and Koji ARIOKA

Institute of Nuclear Safety System, Inc., 64 Sata, Mihama-cho, Mikata-gun, Fukui 919-1205

(Received June 14, 2004 and accepted in revised form October 29, 2004)

Recent studies on stress corrosion cracking (SCC) behaviors of austenitic stainless steels in hydrogenated high-temperature water show that low potential SCC (LPSCC) can occur on cold-worked SUS 316 stainless steel (hereinafter, 316SS). In this study, oxide films and crack tips on cold-worked 316SS exposed to hydrogenated high-temperature water were characterized using analytical transmission electron microscopy (ATEM), grazing incidence X-ray diffraction (GIXRD) and Auger electron spectroscopy (AES) in order to study the corrosion and SCC behaviors of these films and crack tips. A double layer structure was identified for the oxide film after a constant extension rate tensile (CERT) test. The outer layer was composed of large particles (0.2–3 μm) of Fe_3O_4 and the inner layer consisted mainly of fine particles (~10 nm) of $FeCr_2O_4$. In addition, nickel enrichment was identified at the metal/oxide interface. Particles of Fe_3O_4 were also identified on the crack walls. These results indicate that the same electrochemical reactions had occurred inside and outside the crack. The crack tip area was filled with corrosion products of a chromium-rich oxide. In addition, nickel enrichment was observed at the crack tip. The formation of the nickel-enriched phase indicates that a selective dissolution reaction of iron and chromium occurred at the front of the LPSCC crack.

KEYWORDS: stress corrosion cracking, crack tip, oxide film, SUS316, pressurized water reactors, TEM

I. Introduction

Low potential stress corrosion cracking (LPSCC) of nickel-based Alloy600 is known to be an important degradation phenomenon in pressurized water reactors (PWRs). However, the susceptibility of unsensitized austenitic stainless steels to LPSCC is considered quite low, because this phenomenon has not yet been reported in actual PWR plants, except in cases of irradiation assisted stress corrosion cracking (IASCC). However, recent studies using constant extension rate tensile (CERT) testing revealed that cold-worked 316SS is susceptible to LPSCC.[1–3] In one of those reports, Arioka *et al.*[2] found that water chemistry conditions influence the LPSCC of 316SS. This suggests that dissolution or oxidation should affect susceptibility to LPSCC. Therefore, knowledge of the corrosion reaction at crack tips of LPSCC is important for understanding the mechanism of crack propagation.

In recent years, oxide films and SCC crack tips of Alloy600 have been observed directly by transmission electron microscopy (TEM).[4–7] The results clearly show that oxide films have a doble-layer structure and there are oxidized zones along grain boundaries on the crack tips. In addition, it was reported that the corrosion products in the inner layer are the same as those formed on the crack tips. Thomas *et al.*[8,9] used TEM to directly observe crack tips for IASCC of irradiated austenitic stainless steels. On the other hand, no literature has been published on the LPSCC of unirradiated austenitic stainless steel.

Another way to clarify the mechanism underlying SCC—by characterizing the oxide films formed on austenitic stainless steels has been carried out for many years,[10–17] because the chemical and physical properties of oxide films are thought to play important roles in the cracking process, especially in its initiation stage.[18–20] According to the results of those studies, oxide film formed on stainless steel in high-temperature water has a double-layer structure. In particular, the inner layer, which is composed mainly of chromium-rich spinel oxide, is thought to play an important role in corrosion resistance. Therefore, it is necessary to characterize the structure of the inner layer in detail for a deeper understanding of the corrosion mechanism and crack initiation. Cross-sectional observation by TEM is known as an efficient approach to directly observe oxide film, and such studies have been carried out in recent years.[21,22] However, the experimental data collected thus far are insufficient to understand the corrosion mechanism.

In this study, to clarify the roles of dissolution and oxidation on LPSCC of austenitic stainless steels, the microstructures of both the oxide film and crack tip formed on cold-worked 316SS in simulated PWR primary water were analyzed in detail by using TEM, grazing incidence X-ray diffraction (GIXRD) and Auger electron spectroscopy (AES).

II. Experimental Method

1. Sample Preparation

The material used in this study was 316SS, which was solution-treated at 1,150°C for 10 min then water-quenched. The chemical composition is shown in **Table 1**. The crack tip and oxide film used for the analysis were prepared by the CERT test with a high-temperature water circulating system. **Figure 1** shows the morphology of the CERT test specimen. To accelerate the susceptibility to cracking, a

*Corresponding author. Tel. +81-770-37-9111, Fax. +81-770-37-2009, E-mail: terachi@inss.co.jp

Table 1 Chemical composition of the test material (wt%)

C	Cr	Mo	Ni	Mn	Si	P	S	Fe
0.049	17.1	2.1	12.0	1.5	0.45	0.027	0.005	Bal.

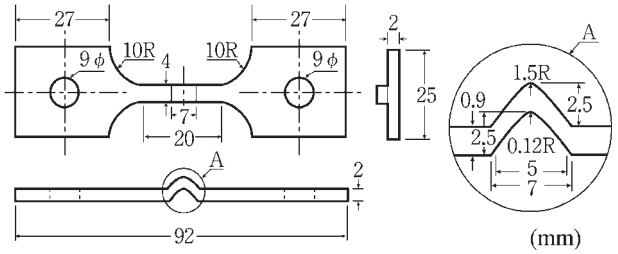

Fig. 1 Specimen dimensions of the CERT test

cold-worked hump was prepared in the gauge section of the specimen.[30] These tests were conducted in the typical chemical environment of simulated PWR primary water chemistries of the middle of the fuel cycle (B: 500 ppm, Li: 2 ppm, DH: 2.75 ppm, 320°C). The extension rate was kept constant throughout the experiment at 0.12 μm/min, and the experimental time was approximately 500 h. The crack morphology was mixed; it initiated in IGSCC then transited to transgranular stress corrosion cracking and finally to ductile. The result of the CERT test was reported previously;[2] in this paper we are not concerned about the SCC growth rate. The crack used for cross-sectional TEM observation is nucleated around the main crack and is approximately 20–100 nm long. Images of the oxide film formed on the specimen surface are shown in **Fig. 2**. The surface of the specimen was covered with octahedral particles that ranged from 0.2 to 3 μm in diameter.

2. Cross-Sectional Sample Preparation

Cross-sectional samples, measuring 2×1×0.3 mm in size and containing cracks and oxide films, were cut from the tested CERT specimen using a diamond saw, taking care not to damage the crack tip or oxide film microstructure. The samples were then mechanically polished to a thickness of 50 μm each. For the TEM analysis, each sample was then processed to a thickness of approximately 0.1 μm using a focused ion beam (FIB) with Ga ion sputtering, as described in our previous paper.[21]

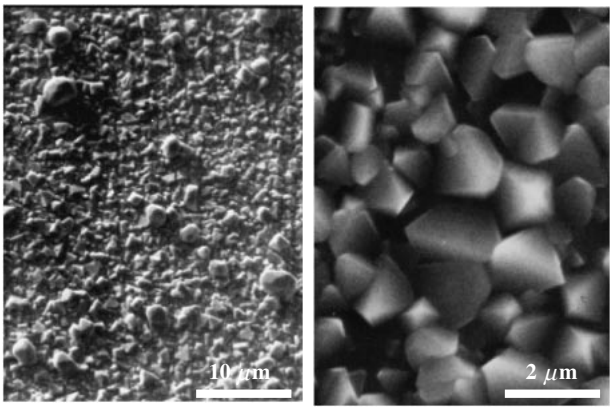

Fig. 2 SEM image of the oxide film composed on the specimen surface after exposure to hydrogenated high temperature water

3. Analysis

The cross-sectional morphology of each crack and oxide film was observed using TEM (Hitachi HF-3000). Energy dispersive spectroscopy (EDS) and micro-electron diffraction analysis were used to determine the chemical composition and structure, respectively. The structure and chemical composition were examined also by GIXRD (Rigaku Rint-2000) analysis and AES (ULVAC-PHISAM680) analysis. Cross-sectional AES analysis was also conducted to confirm the presence of boron in the oxide film.

III. Results

1. Oxide Film

(1) Surface Analysis

Figure 3 shows a typical XRD profile from the gauge section of the tested specimen. All measurement peaks agree with that from the spinel oxide, with the exception of the matrix, and neither a hydroxide peak nor a corundum (Cr_2O_3) peak is observed. Figure 3(a), an inset within Fig. 3, shows the spinel oxide (440) peak in detail. It indicates that the spinel oxide is dominated by Fe_3O_4 and $FeCr_2O_4$.

(2) Cross-Sectional Analysis

Figure 4 shows a cross-sectional TEM image of the oxide film, which has a double-layer structure. The outer layer consists of single crystal particles, 1–2 μm in diameter. On the other hand, the inner layer, approximately 500 nm in depth, consists of fine grains of polycrystal. Several cracks observed in the oxide film were not located on the grain boundaries of the base material in this observation.

Examples of the electron diffraction patterns from the oxide film are shown also in Figs. 4(c), (d). The patterns from both the inner and outer layers were in agreement with the spinel structure. Since the diffraction pattern shows a spot image, the outer layer is considered to be a single crystal and not a polycrystal. In contrast, the structure of the inner layer is identified as having a ring diffraction pattern, confirming that the inner layer consists of fine grains of spinel oxides.

The elemental maps for oxygen, iron, chromium and nickel in a cross-sectional area of the oxide film are shown in **Fig. 5**. The line scan analysis results are shown in **Fig. 6**. The outer layer was composed mainly of iron oxide. Relatively chromium-rich oxide was recognized in the inner layer. These compositional details agree with the results published for oxide films formed in high-temperature pure water.[14] In addition, nickel enrichment was observed at the oxide/metal interface, at up to 70 nm in depth. The quantitative element analysis (point analysis) by EDS, shown in **Fig. 7**, indicates that nickel is enriched in a matrix by more than twice its bulk concentration. Furthermore, we attempted to examine the effect of molybdenum on additional corrosion resistance in simulated PWR primary water. However, as shown in Figs. 6 and 7, molybdenum enrichment was not observed in the oxide film.

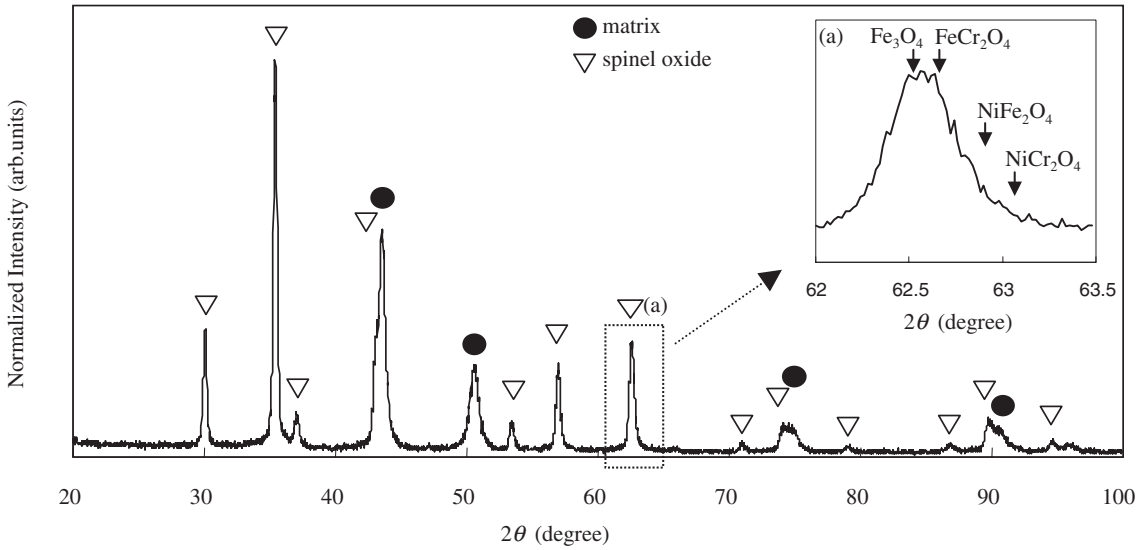

Fig. 3 X-ray diffraction profiles of the specimen using Cu-Kα radiation at incidence angles of less than 1°: (a) Enlargement of the area surrounding the spinel oxide (440) peak

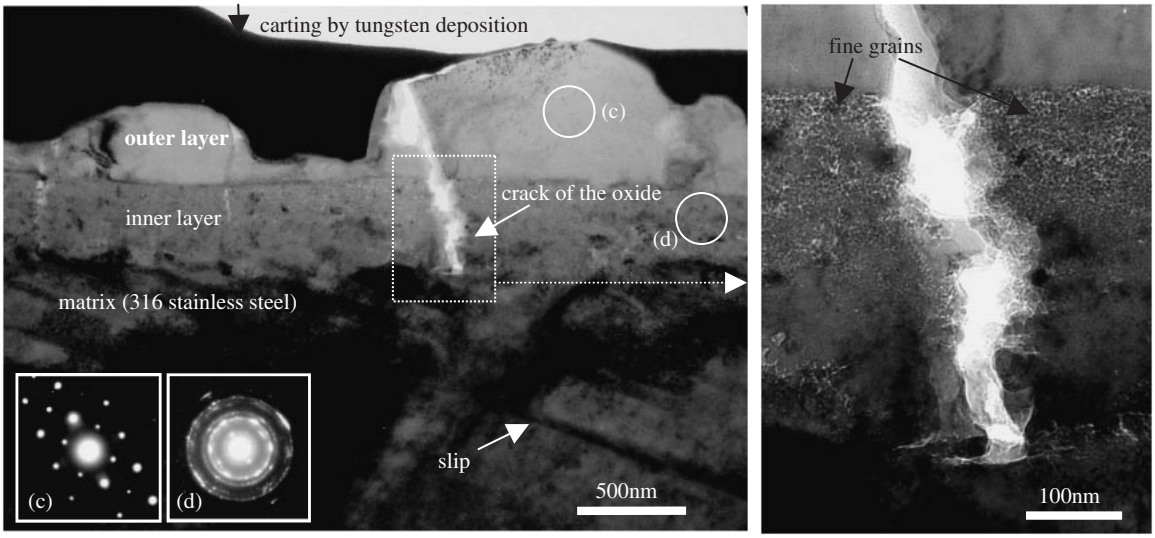

(a) Cross–section image of the oxide film

(b) The enlargement of the crack of the oxide film

Fig. 4 Cross-sectional TEM image of the oxide film composed on the specimen surface formed under hydrogenated high-temperature water: (c) Outer layer diffraction pattern with spot from spinel oxide, (d) Diffraction pattern with rings from fine grained spinel oxide

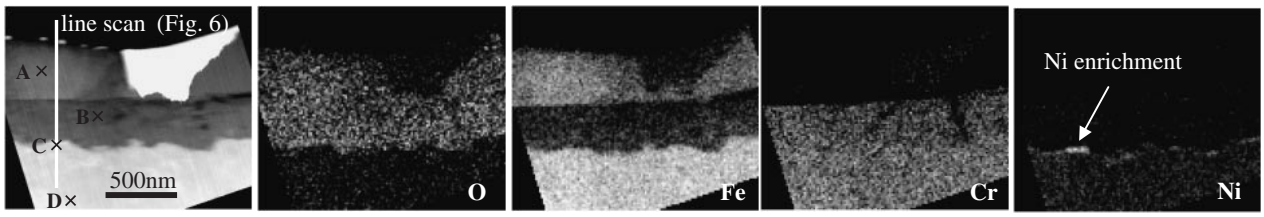

Fig. 5 Elemental maps of the oxide film obtained by EDS. Marked areas refer to: outer layer (A), inner layer (B), outer layer/inner layer interface (C), matrix (D), as shown in Fig. 7

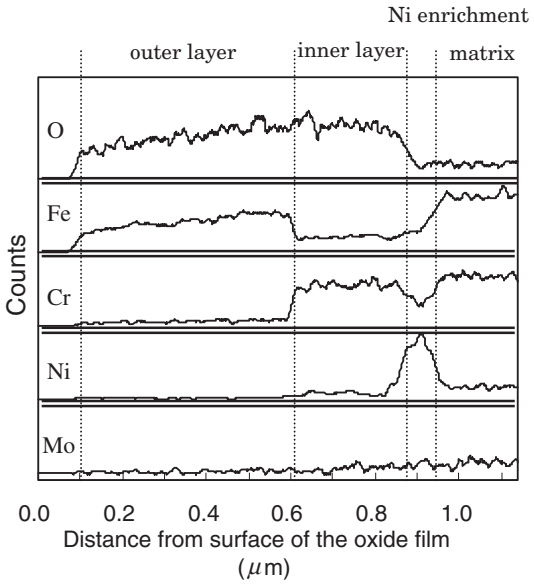

Fig. 6 EDS line scan profiles across the oxide film
The analysis area is shown in Fig. 5.

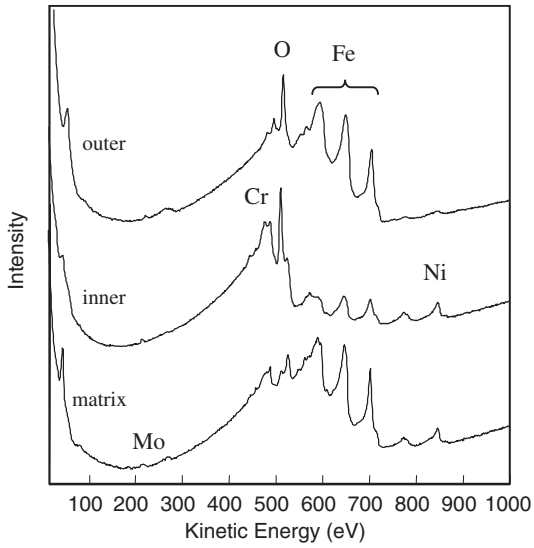

Fig. 8 AES analysis of the cross-sectional oxide film

Figure 8 shows AES spectra from the outer and inner oxide films and the matrix of the cross-sectional sample. At approximately 178 eV, peaks of boron, whose detection limit is approximately 0.1 at.%, were not observed in either the outer or inner layer of the oxide.

2. Crack

(1) Crack-Initiation Area

An SEM image of the initiation area of intergranular cracking is shown in **Fig. 9**. Although grown octahedral particles occupied the surface of the specimen, only smaller particles were observed on the fracture facet. The quantity of corrosion products formed on each granular facet was inconsistent with that formed on the same crack.

(2) Cross-Sectional Analysis

Figure 10 shows a cross-sectional SEM image of a crack. The grained corrosion products are formed on only one side of the crack surface. Additionally, slip step-like patterns were observed on the fracture surface.

Figure 11 provides AES elemental maps for oxygen, iron,

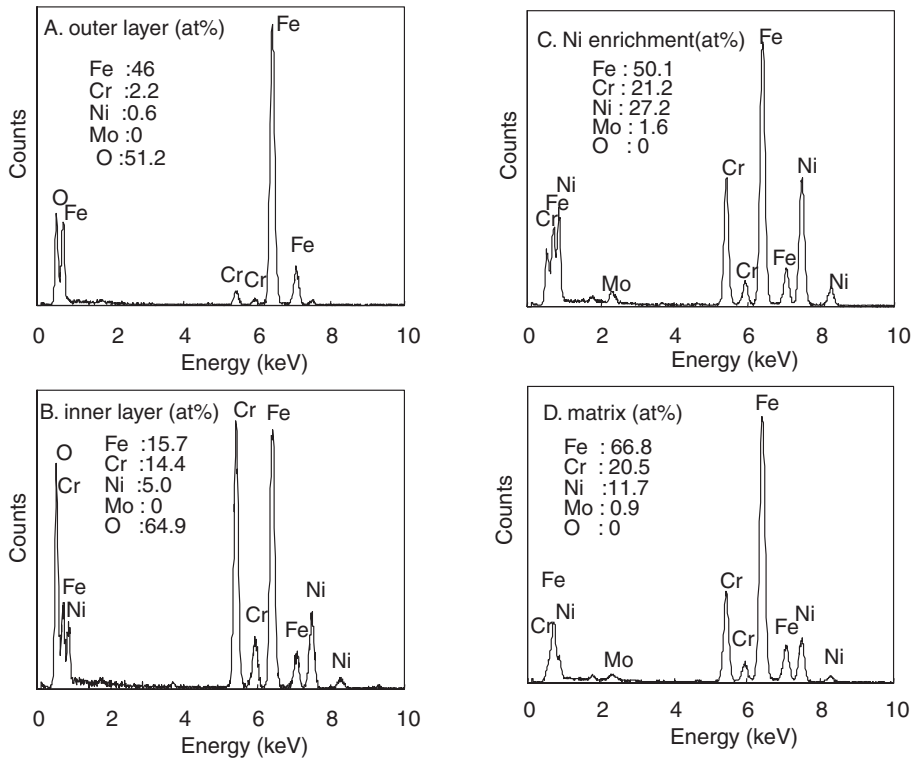

Fig. 7 Chemical compositions of the oxide film with matrix obtained by EDS. The analysis area is marked on Fig. 5

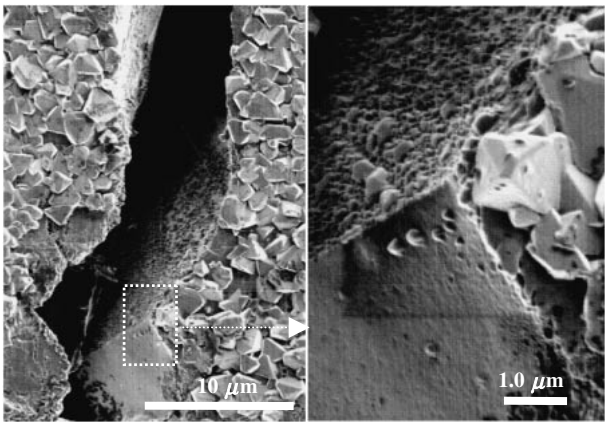

Fig. 9 SEM image of the initiation stage of the crack

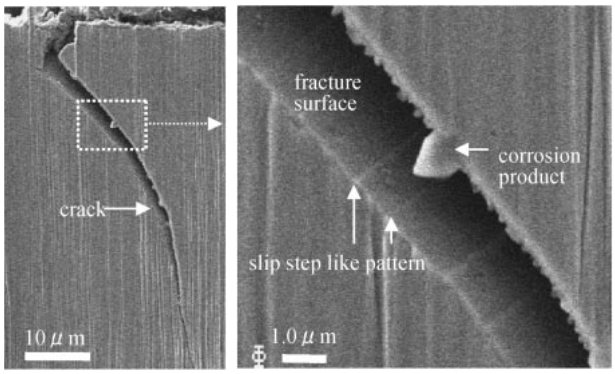

Fig. 10 SEM cross-sectional image of the crack

chromium and nickel in the cross-sectional area of the crack. They show that the oxide film on the upper facet consists of an iron-rich outer layer and a chromium-rich inner layer of oxide, in agreement with the characteristics of the oxide film formed on the specimen surface.

Figure 12 shows a cross section of the LPSCC crack formed under simulated PWR primary water conditions. The whole crack image shown in Fig. 12(a) indicates differences in the levels formed on the surface of the specimen. This finding suggests that grain boundary sliding has affected the cracking process, especially during the initiation stage. A low-magnification TEM image of the crack tip is shown in Fig. 12(b). Corrosion products are observed in the crack, which consists of a spinel structure, as determined by electron diffraction (as shown in Fig. 12(b)). Furthermore, the EDS spectrum shows the following composition (at.%): Fe, 39.1%; Cr, 2.3%; Ni, 2.6%; Mo, not detected;

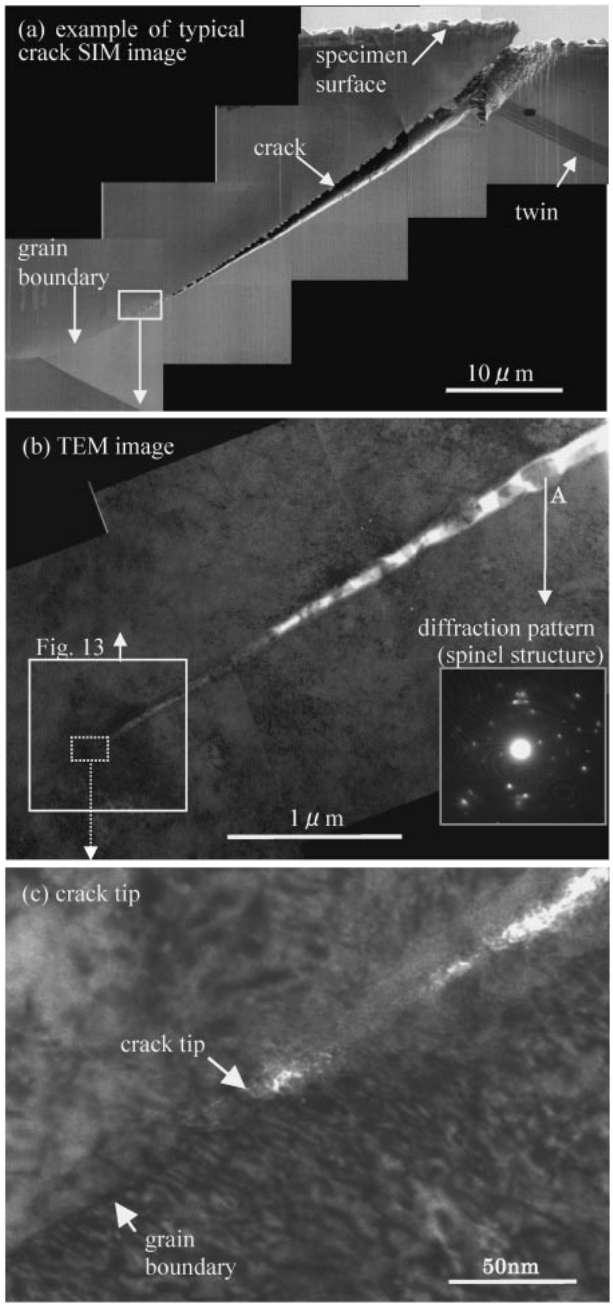

Fig. 12 Cross-section crack morphology: (a) SEM image of a typical crack, (b) low-magnification TEM image, (c) TEM image of the crack tip region

and O, 56.1% (at.%). Thus, the main corrosion products are assumed to be Fe_3O_4, which grows by the deposition of iron.

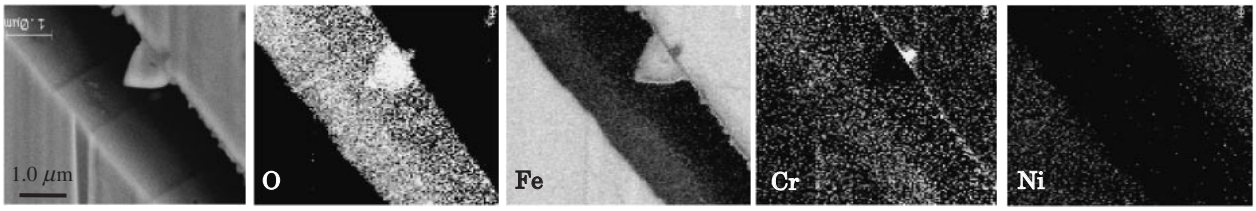

Fig. 11 Elemental maps of the cross-section of the crack obtained by AES

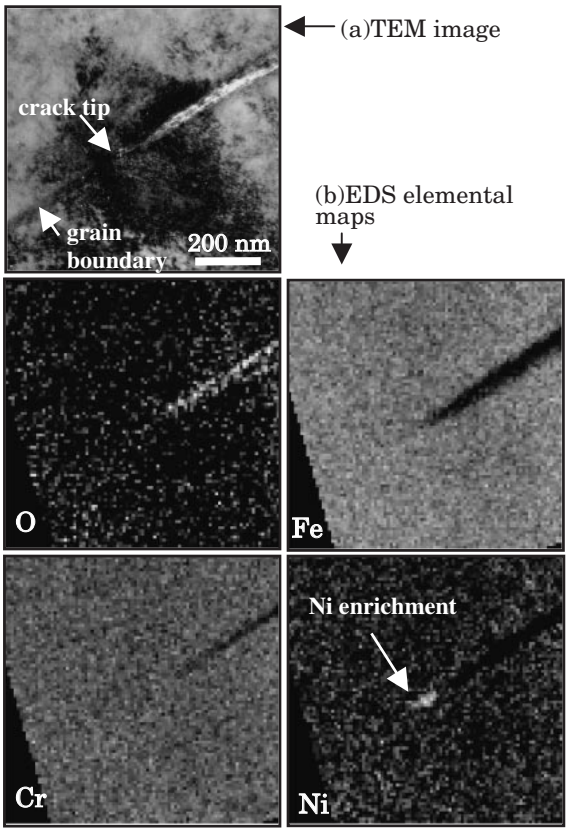

Fig. 13 TEM image of the crack tip region (a: enlarged region within Fig. 12), and EDS elemental maps from part of the sample shown in (a)

Figure 13 shows a TEM image and EDS elemental maps of the crack tip. The crack is filled with corrosion products. Additionally, metallic nickel enrichment at the crack tip is confirmed, as shown in Fig. 13(b). The chemical composition of the nickel enrichment area was measured by EDS as Fe, 56.7%; Cr, 21.9%; Ni, 15.1%; Mo, 6.4%; and O, not detected (at.%).

IV. Discussion

1. Oxide Film Characterization

The results of the oxide film characterization, formed in hydrogenated high-temperature water, are illustrated in **Fig. 14**.

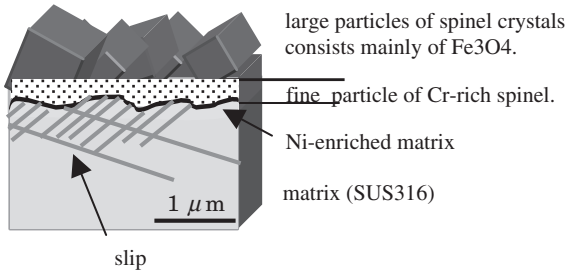

Fig. 14 Schematic representation of the oxide film formed on the surface of the CERT specimen exposed to simulated PWR primary water

The results by electron diffraction and EDS indicate that the outer oxide is composed of an iron-rich oxide with a spinel structure, which was supported by XRD analysis. Therefore, it is concluded that the outer layer is composed mainly of Fe_3O_4 due to the redeposition of iron. On the other hand, the inner oxide layer is composed of chromium-rich oxide with a spinel structure. The results of electron diffraction and TEM observation suggest that the inner layer is composed of fine grains.

The corrosion potential of 316SS under the PWR primary environment was reported to be approximately −830 mV.[23,24] Thermodynamically, the most stable product for SUS316 is $FeCr_2O_4$.[25] These considerations are consistent with the present results, which show that the inner layer consists mainly of iron and chromium spinels.

A cross-sectional observation reveals the enrichment of metallic nickel at the oxide/metal interface. This result is consistent with the oxide film formed on the nickel-based alloy under the same condition as the present authors reported previously.[26]

The material used in this study was 316SS, which differs from 304SS primarily in that molybdenum is added to the former to reduce corrosion. For this reason, it was thought that molybdenum might play an important role in corrosion resistance by protecting the oxide film. However, no molybdenum concentrates in the oxide film were observed. Arioka *et al.*[27] reported that molybdenum does not serve to mitigate the LPSCC susceptibility of austenitic stainless steels.

2. Crack Tip Morphology and Cracking Mechanism

A cross-sectional view of the LPSCC crack is schematically shown in **Fig. 15**. From the microstructural analysis, it can be deduced that Fe_3O_4 precipitated at the crack wall and that the crack tip filled with corrosion products consisting mainly of chromium-rich oxide. Thus, the oxide film on the crack wall has the same structure as that formed on the specimen surface except for film thickness. This suggests that there is no large potential gradient between the surface of the specimen and the inside of the crack, in such a hydrogenated PWR primary environment. This result is inconsistent with that in an oxygenated condition such as that of boiling water reactors (BWR). The potential gradient in BWR environments is confirmed by the analytic result that the surface oxide consists mainly of α-Fe_2O_3, even though Fe_3O_4

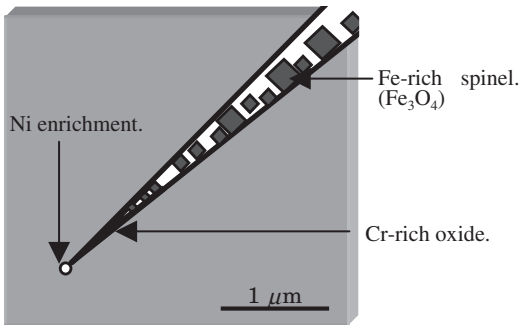

Fig. 15 Schematic representation of the crack tip formed in the CERT specimen under simulated PWR primary water

was observed inside the crack.[9,16] In this regard, the mechanism of LPSCC is assumed to differ from the typical active path corrosion model.

From the EDS analysis results, metallic nickel enrichment was observed ahead of the crack tip. One of the explanations for the generation of nickel enrichment is the difference in the thermodynamic stability of the component elements. It is reasonable to suppose that chromium and iron are selectively dissolved and that nickel remains at the reaction front. Another explanation for nickel enrichment is that diffusion rates differ, although the difference is not large enough to account for the observed behavior. Nevertheless, it has been reported that the diffusion velocity of nickel is slower than that of chromium and iron. Although the mechanism of nickel enrichment is not clear, this result reveals that selective dissolution of iron and chromium occurred at the crack tip.

In nickel-based alloy, oxidized zones along grain boundaries on the crack tips in a simulated PWR environment were reported.[4–6] Therefore, to examine the possibility of internal oxidation as a proposed LPSCC mechanism, detailed observations of the crack tip were performed. However, clear evidence of internal oxidation was not detected in this study.

Was *et al.*[28,29] studied the correlation between intergranular (IG) cracking and creep behaviors for nickel-based alloy and found that the environment, through the presence of hydrogen, enhanced IG cracking. Additionally, Arioka *et al.*[1] reported that grain boundary sliding occurred on austenitic stainless steel at a PWR operating temperature. In this regard, the LPSCC phenomena in austenitic stainless steel are assumed to be influenced by grain boundary sliding. In this study, slip step-like patterns were observed on the crack surface by cross-sectional analysis using SEM, which seems to indicate that slip phenomena such as grain boundary sliding affect crack propagation.

The LPSCC on SUS316 might be influenced by slip and dissolution. However, several studies have indicated that hydrogen entering the material plays an important role in LPSCC in nickel-based alloys.[30,31] Therefore, the role of electrochemical reactions (anodic and cathodic reactions) may be one not only of dissolution but also of a source of hydrogen. Although the dependence of susceptibility to LPSCC on electrochemical reactions is not clear, the preliminary conclusion is that the cracking process can be expressed in a similar manner as in the slip dissolution model.

V. Conclusion

In order to clarify the role of dissolution and oxidation on LPSCC of austenitic stainless steels, the microstructures of the oxide film and crack tip formed on cold-worked SUS316 in simulated PWR primary water (B: 500 ppm, Li: 2 ppm, DH 2.75 ppm, 320°C) were analyzed in detail. The following conclusions were obtained.

(1) The oxide film consists of double layers. The outer layer is composed mainly of granular Fe_3O_4, and the inner layer consists of fine grains of chromium-rich spinel oxide. Nickel enrichment was observed at the metal/oxide interface.
(2) The oxide on the crack wall through the crack tip has the same structure as that on the specimen surface. It is suggested that a large potential gradient does not exist within or outside the crack in this case.
(3) The crack tip was filled with corrosion products of a chromium-rich oxide. Enrichment of nickel was identified at the crack tip. Clear evidence of grain boundary oxidation was not observed ahead of the crack tip. These results suggest that LPSCC advanced along with anodic and cathodic reactions.
(4) Slip step-like patterns were observed on the crack surface by cross-sectional analysis, indicating that LPSCC propagates along with slip phenomena.
(5) It was observed that the crack tip was filled with corrosion products composed of a chromium-rich oxide, and enrichment of nickel was observed ahead of the crack tip.

Acknowledgments

The authors wish to acknowledge the financial support provided by Kansai Electric Power Co., Inc. for this study. The reliable experimental support provided by the staff at our Institute and that of K. Murakami, K. Tsujii, and M. Hirao of Kanden Kogyo Co., Ltd., are also acknowledged. We are also grateful to Dr. T. Yamada of this Institute for technical support with the TEM analysis.

References

1) K. Arioka, Y. Kaneshima, T. Yamada, T. Terachi, "Influence of boric acid, hydrogen concentration and grain boundary carbide on IGSCC behaviors of SUS 316 under PWR primary water," *Proc. 11th Int. Symp. Environmental Degradation of Materials in Nuclear Power Systems Water Reactors*, Washington, Aug. 10–14, 2003, (2003).
2) K. Arioka, "Effect of temperature, hydrogen and boric acid concentration on IGSCC susceptibility of annealed 316 stainless steel," *Proc. Fontebraud 5*, Sept. 23–27, 2002, (2002).
3) N. Totsuka, Z. Szklarska-Smialowska, "Hydrogen induced IGSCC of two unsensitized austenitic stainless steels in high temperature water," *Corrosion*, **44**, 124 (1988).
4) S. M. Bruemmer, "High-resolution characterization of intergranular attack and stress corrosion cracking of Alloy600 in high temperature primary water," *Corrosion*, **56**[6], 572 (2000).
5) S. Lozano-Perez, J. M. Titchmarsh, "Observation of the microstructure of crack tips in Inconel 600," *Proc. INSS 10th Anniversary*, May 27–29, 2002, (2002).
6) K. Fujii, K. Fukuya, N. Nakajima, "Characterization of SCC crack tip and hydrogen distribution in Alloy600," *INSS J.*, **8**, 143 (2002), [in Japanese].
7) M. Kanazaki, T. Noda, H. Anada, "Behavior and role of hydrogen and oxygen in PWSCC of Alloy600MA and Alloy600TT," *Proc. 11th Int. Symp. Environmental Degradation of Materials in Nuclear Power Systems Water Reactors*, Washington, Aug. 10–14, 2003, (2003).
8) L. E. Thomas, S. M. Bruemmer, "Analytical transmission electron microscopy characterization of stress corrosion cracks in irradiated type 316 stainless steel core component," *Proc. Fontevraud 5*, Sept. 23–27, 2002, (2002).
9) L. E. Thomas, S. M. Bruemmer, "Microstructural and microchemical characterization of intergranular stress corrosion

cracks in irradiated type 304SS removed from a BWR top guide," *Proc. 11th Int. Conf. Environmental Degradation of Materials in Nuclear Power Systems Water Reactors*, NACE, (2003).
10) R. L. Tapping, R. D. Davidson, E. Mcalpine, "The composition and morphology of oxide films formed on type 304 stainless steel in lithiated high-temperature water," *Corrosion Sci.*, **26**[8], 563 (1986).
11) D. H. Lister, R. D. Davidson, E. Mcalpine, "The mechanism and kinetics of corrosion product release from stainless steel in lithiated high-temperature water," *Corrosion Sci.*, **27**[2], 113 (1987).
12) J. Robertson, "The mechanism of high temperature aqueous corrosion of stainless steels," *Corrosion Sci.*, **32**[4], 443 (1991).
13) Z. S. Smialowska, K.-C. Chou, Z. Xia, "The composition and properties of oxide films on type 304 stainless steel on exposure to lithiated water at 100–350°C," *Corrosion Sci.*, **32**[5/6], 609 (1991).
14) Y. J. Kim, "Characterization of the oxide film formed on type 316 stainless steel in 288°C water in cyclic normal and hydrogen water chemistries," *Corrosion*, **51**[11], 849 (1995).
15) B. Stelleag, "The mechanism of oxide film formation on austenitic stainless steels in high-temperature water," *Corrosion Sci.*, **40**[2/3], 337 (1998).
16) Y. J. Kim, "Analysis of oxide film formed on type 304 stainless steel in 288°C water containing oxygen, hydrogen, and hydrogen peroxide," *Corrosion*, **55**[1], 81 (1999).
17) S. E. Ziemniak, M. Hanson, "Corrosion behavior of 304 stainless steel in high temperature hydrogenated water," *Corrosion Sci.*, **44**, 2209 (2002).
18) H. Kawamura, H. Hirano, K. Yamaoka, "The effect of zinc addition to simulated PWR primary water on the PWSCC resistance, crack growth rate and surface oxide film characteristics of prefilmed Alloy600," *Corrosion 98*, Paper 141, (1998).
19) J. F. Chen, S. Souma, S. Matsuda, "Relationship between nature of surface films and susceptibility to intergranular stress corrosion cracking on sensitized SUS 304 stainless steel in high-temperature aqueous solutions," *Boshoku Gijutsu*, **38**, 203 (1989), [in Japanese].
20) K. Fujiwara, H. Tomari, K. Shimogori, "An electrochemical study on the role of dissolved oxygen in the IGSCC of sensitized type 304 stainless steel in dilute Na_2SO_4 solution at 285C," *Corrosion*, **38**[2], 69 (1982).
21) K. Fujii, K. Fukuya, N. Nakajima, "Evaluation of surface oxidation mechanism of Alloy600 in simulated primary water of pressurized water reactors using analytical transmission electron microscopy," *Trans. At. Energy Soc. Jpn.*, **1**[2], 127 (2002), [in Japanese].
22) Y. Nemoto, Y. Miwa, M. Kikuchi, "Development of analytical method and study about microstructure of oxide films on stainless steel," *J. Nucl. Sci. Technol.*, **39**[9], 996 (2002).
23) K. Arioka, T. Terachi, "Influence of dissolved oxygen, hydrogen and Cr contents on the potential under PWE water," *Preprints 2002 Ann. Meeting of At. Energy Soc. Japan*, Kobe, Mar. 27–29, 2002, E30, p. 737 (2002), [in Japanese].
24) A. Bertuch, K. Arioka, D. D. Macdonald, "Modeling the corrosion behaviors of the heat transport circuits of light water nuclear reactors," *Proc. 6th Int. Conf. Environmental Degradation of Materials in Nuclear Power Systems Water Reactors*, NACE, p. 905 (1993).
25) B. Beverskog, I. Pujgdomenech, "Pourbaix diagrams for the ternary system of iron–chromium–nickel," *Corrosion*, **55**[11], 1077 (1999).
26) T. Terachi, N. Totsuka, T. Yamada, *et al.*, "Influence of dissolved hydrogen on structure of oxide film on Alloy600 formed in primary water of pressurized water reactors," *J. Nucl. Sci. Technol.*, **40**[7], 509, (2003).
27) K. Arioka, T. Yamada, T. Terachi "Influence of grain boundary carbide and alloy compositions on IGSCC of SUS316 and SUS304," *Proc. Zairyo-to-Kankyo 2004*, Tokyo, (2004), [in Japanese].
28) T. M. Angeliu, D. J. Paraventi, G. S. Was, "Creep and intergranular cracking behavior of nickel–chromium–iron–carbon Alloys in 360°C water," *Corrosion Sci.*, **51**[11], 837 (1995).
29) B. Capell, L. Fournier, G. Was, "Intergranular cracking behavior of Ni–16Cr–9Fe–C alloys in hydrogenated steam," *Proc. 10th Int. Conf. Environmental Degradation of Materials in Nuclear Power Systems Water Reactors*, NACE, (2001).
30) N. Totsuka, E. Lunarska, G. Cragnolomo, Z. Szklarska-Smialowska, "Effect of hydrogen on the intergranular stress corrosion cracking of Alloy600 in high temperature aqueous environment," *Corrosion*, **43**, 505 (1987).
31) M. M. Hall, Jr., D. M. Symons, "Hydrogen assisted creep fracture model for low potential stress corrosion cracking of Ni–Cr–Fe alloys," *Proc. TMS 2001 Symp. on Chemistry and Electrochemistry of SCC*, New Orleans, (2001).